

# Wavelength swept amplified spontaneous emission source

Christoph M. Eigenwillig, Benjamin R. Biedermann, Wolfgang Wieser  
and Robert Huber\*

*Lehrstuhl für BioMolekulare Optik, Fakultät für Physik, Ludwig-Maximilians-Universität München  
Oettingenstr. 67, 80538 Munich, Germany*

*\* [Robert.Huber@Physik.Uni-Muenchen.DE](mailto:Robert.Huber@Physik.Uni-Muenchen.DE)*

**Abstract:** We present a new, alternative approach to realize a wavelength swept light source with no fundamental limit to sweep speed. Amplified spontaneous emission (ASE) light alternately passes a cascade of optical gain elements and tunable optical bandpass filters. We show that for high sweep speeds, the control signal for the different filters has to be applied with a defined, precise phase delay on the order of nanoseconds, to compensate for the light propagation time between the filters and ensure optimum operation. At a center wavelength of 1300 nm sweep rates of 10 kHz, 100 kHz and 340 kHz over a sweep range of 100 nm full width and an average power of 50 mW are demonstrated. For application in optical coherence tomography (OCT), an axial resolution of 12  $\mu\text{m}$  (air), a sensitivity of 120 dB (50 mW) and a dynamic range of 50 dB are achieved and OCT imaging is demonstrated. Performance parameters like coherence properties and relative intensity noise (RIN) are quantified, discussed and compared to the performance of Fourier Domain Mode Locked (FDML) lasers. Physical models for the observed difference in performance are provided.

©2009 Optical Society of America

**OCIS codes:** (140.3600) Lasers, tunable; (110.4500) Imaging systems: Optical coherence tomography; (120.3180) Instrumentation, measurement, and metrology: Interferometry; (110.4280) Noise in imaging systems; (120.2230) Instrumentation, measurement, and metrology, Fabry-Perot; (120.2440) Instrumentation, measurement, and metrology: Filters.

---

## References and links

1. D. Huang, E. A. Swanson, C. P. Lin, J. S. Schuman, W. G. Stinson, W. Chang, M. R. Hee, T. Flotte, K. Gregory, C. A. Puliafito, and J. G. Fujimoto, "OPTICAL COHERENCE TOMOGRAPHY," *Science* **254**(5035), 1178–1181 (1991), <http://www.sciencemag.org/cgi/content/abstract/sci:254/5035/1178>.
2. G. Häusler, and M. W. Lindner, "Coherence Radar and Spectral Radar—New Tools for Dermatological Diagnosis," *J. Biomed. Opt.* **3**(1), 21–31 (1998), <http://dx.doi.org/10.1117/1.429899>.
3. A. F. Fercher, C. K. Hitzenberger, G. Kamp, and S. Y. Elzaiat, "MEASUREMENT OF INTRAOCULAR DISTANCES BY BACKSCATTERING SPECTRAL INTERFEROMETRY," *Opt. Commun.* **117**(1-2), 43–48 (1995), [http://dx.doi.org/10.1016/0030-4018\(95\)00119-S](http://dx.doi.org/10.1016/0030-4018(95)00119-S).
4. R. Leitgeb, C. K. Hitzenberger, and A. F. Fercher, "Performance of fourier domain vs. time domain optical coherence tomography," *Opt. Express* **11**(8), 889–894 (2003), <http://www.opticsinfobase.org/oe/abstract.cfm?URI=oe-11-8-889>.
5. J. F. de Boer, B. Cense, B. H. Park, M. C. Pierce, G. J. Tearney, and B. E. Bouma, "Improved signal-to-noise ratio in spectral-domain compared with time-domain optical coherence tomography," *Opt. Lett.* **28**(21), 2067–2069 (2003), <http://www.opticsinfobase.org/ol/abstract.cfm?URI=ol-28-21-2067>.
6. M. A. Choma, M. V. Sarunic, C. H. Yang, and J. A. Izatt, "Sensitivity advantage of swept source and Fourier domain optical coherence tomography," *Opt. Express* **11**(18), 2183–2189 (2003), <http://www.opticsinfobase.org/oe/abstract.cfm?URI=oe-11-18-2183>.
7. S. H. Yun, G. J. Tearney, J. F. de Boer, N. Iftimia, and B. E. Bouma, "High-speed optical frequency-domain imaging," *Opt. Express* **11**(22), 2953–2963 (2003), <http://www.opticsinfobase.org/oe/abstract.cfm?URI=oe-11-22-2953>.
8. S. H. Yun, G. J. Tearney, J. F. de Boer, and B. E. Bouma, "Motion artifacts in optical coherence tomography with frequency-domain ranging," *Opt. Express* **12**(13), 2977–2998 (2004), <http://www.opticsinfobase.org/oe/abstract.cfm?URI=oe-12-13-2977>.

9. S. Moon, and D. Y. Kim, "Ultra-high-speed optical coherence tomography with a stretched pulse supercontinuum source," *Opt. Express* **14**(24), 11575–11584 (2006), <http://www.opticsinfobase.org/oe/abstract.cfm?URI=oe-14-24-11575>.
10. W. Y. Oh, S. H. Yun, B. J. Vakoc, G. J. Tearney, and B. E. Bouma, "Ultrahigh-speed optical frequency domain imaging and application to laser ablation monitoring," *Appl. Phys. Lett.* **88**(10), 103902 (2006), <http://link.aip.org/link/?APPLAB/88/103902/1>.
11. R. Huber, D. C. Adler, and J. G. Fujimoto, "Buffered Fourier domain mode locking: Unidirectional swept laser sources for optical coherence tomography imaging at 370,000 lines/s," *Opt. Lett.* **31**(20), 2975–2977 (2006), <http://www.opticsinfobase.org/ol/abstract.cfm?URI=ol-31-20-2975>.
12. R. Huber, M. Wojtkowski, K. Taira, J. G. Fujimoto, and K. Hsu, "Amplified, frequency swept lasers for frequency domain reflectometry and OCT imaging: design and scaling principles," *Opt. Express* **13**(9), 3513–3528 (2005), <http://www.opticsinfobase.org/oe/abstract.cfm?URI=oe-13-9-3513>.
13. R. Huber, M. Wojtkowski, and J. G. Fujimoto, "Fourier Domain Mode Locking (FDML): A new laser operating regime and applications for optical coherence tomography," *Opt. Express* **14**(8), 3225–3237 (2006), <http://www.opticsinfobase.org/oe/abstract.cfm?URI=oe-14-8-3225>.
14. T. J. Eom, V. A. Tougbaev, B. A. Yu, W. Shin, Y. L. Lee, and D. K. Ko, "Narrowband wavelength selective detector applicable SD-OCT based on Fabry-Perot tunable filter and balanced photoreceiver," in *Coherence Domain Optical Methods and Optical Coherence Tomography in Biomedicine XII*, (SPIE, 2008), 68470R–68471. [http://spie.org/x648.html?product\\_id=766436](http://spie.org/x648.html?product_id=766436)
15. G. Y. Liu, A. Mariampillai, B. A. Standish, N. R. Munce, X. J. Gu, and I. A. Vitkin, "High power wavelength linearly swept mode locked fiber laser for OCT imaging," *Opt. Express* **16**(18), 14095–14105 (2008), <http://www.opticsinfobase.org/oe/abstract.cfm?URI=oe-16-18-14095>.
16. Y. X. Mao, C. Fluerau, S. Sherif, and S. D. Chang, "High performance wavelength-swept laser with mode-locking technique for optical coherence tomography," *Opt. Commun.* **282**(1), 88–92 (2009), <http://dx.doi.org/10.1016/j.optcom.2008.09.059>.
17. M. Y. Jeon, J. Zhang, and Z. P. Chen, "Characterization of Fourier domain mode-locked wavelength swept laser for optical coherence tomography imaging," *Opt. Express* **16**(6), 3727–3737 (2008), <http://www.opticsinfobase.org/oe/abstract.cfm?URI=oe-16-6-3727>.
18. M. Y. Jeon, J. Zhang, Q. Wang, and Z. Chen, "High-speed and wide bandwidth Fourier domain mode-locked wavelength swept laser with multiple SOAs," *Opt. Express* **16**(4), 2547–2554 (2008), <http://www.opticsinfobase.org/oe/abstract.cfm?URI=oe-16-4-2547>.
19. E. J. Jung, C. S. Kim, M. Y. Jeong, M. K. Kim, M. Y. Jeon, W. Jung, and Z. P. Chen, "Characterization of FBG sensor interrogation based on a FDML wavelength swept laser," *Opt. Express* **16**(21), 16552–16560 (2008), <http://www.opticsinfobase.org/oe/abstract.cfm?URI=oe-16-21-16552>.
20. Y. Wang, W. Liu, J. Fu, and D. Chen, "Quasi-distributed fiber Bragg grating sensor system based on a Fourier domain mode locking fiber laser," *Laser Phys.* **19**(3), 450–454 (2009), <http://www.springerlink.com/content/p300147134334266/>.
21. D. Chen, C. Shu, and S. He, "Multiple fiber Bragg grating interrogation based on a spectrum-limited Fourier domain mode-locking fiber laser," *Opt. Lett.* **33**(13), 1395–1397 (2008), <http://www.opticsinfobase.org/ol/abstract.cfm?URI=ol-33-13-1395>.
22. M. J. R. Heck, A. Renault, E. Bente, Y. S. Oei, M. K. Smit, K. S. E. Eikema, W. Ubachs, S. Anantathanasarn, and R. Notzel, "Passively Mode-Locked 4.6 and 10.5 GHz Quantum Dot Laser Diodes Around 1.55  $\mu\text{m}$  With Large Operating Regime," *IEEE J. Sel. Top. Quantum Electron.* **15**, 634–643 (2009), [http://ieeexplore.ieee.org/xpl/freeabs\\_all.jsp?isnumber=5068462&arnumber=4982709&count=68&index=19](http://ieeexplore.ieee.org/xpl/freeabs_all.jsp?isnumber=5068462&arnumber=4982709&count=68&index=19).
23. D. C. Adler, R. Huber, and J. G. Fujimoto, "Phase-sensitive optical coherence tomography at up to 370,000 lines per second using buffered Fourier domain mode-locked lasers," *Opt. Lett.* **32**(6), 626–628 (2007), <http://www.opticsinfobase.org/ol/abstract.cfm?URI=ol-32-6-626>.
24. D. C. Adler, Y. Chen, R. Huber, J. Schmitt, J. Connolly, and J. G. Fujimoto, "Three-dimensional endomicroscopy using optical coherence tomography," *Nat. Photonics* **1**(12), 709–716 (2007), <http://www.nature.com/nphoton/journal/v1/n12/abs/nphoton.2007.228.html>.
25. D. C. Adler, S. W. Huang, R. Huber, and J. G. Fujimoto, "Photothermal detection of gold nanoparticles using phase-sensitive optical coherence tomography," *Opt. Express* **16**(7), 4376–4393 (2008), <http://www.opticsinfobase.org/oe/abstract.cfm?URI=oe-16-7-4376>.
26. D. C. Adler, J. Stenger, I. Gorczynska, H. Lie, T. Hensick, R. Spronk, S. Wolohojian, N. Khandekar, J. Y. Jiang, S. Barry, A. E. Cable, R. Huber, and J. G. Fujimoto, "Comparison of three-dimensional optical coherence tomography and high resolution photography for art conservation studies," *Opt. Express* **15**(24), 15972–15986 (2007), <http://www.opticsinfobase.org/oe/abstract.cfm?URI=oe-15-24-15972>.
27. P. M. Andrews, Y. Chen, M. L. Onozato, S. W. Huang, D. C. Adler, R. A. Huber, J. Jiang, S. E. Barry, A. E. Cable, and J. G. Fujimoto, "High-resolution optical coherence tomography imaging of the living kidney," *Lab. Invest.* **88**(4), 441–449 (2008), <http://www.nature.com/labinvest/journal/v88/n4/full/labinvest20084a.html>.
28. T. Bajraszewski, M. Wojtkowski, M. Szkulmowski, A. Szkulmowska, R. Huber, and A. Kowalczyk, "Improved spectral optical coherence tomography using optical frequency comb," *Opt. Express* **16**(6), 4163–4176 (2008), <http://www.opticsinfobase.org/oe/abstract.cfm?URI=oe-16-6-4163>.
29. B. R. Biedermann, W. Wieser, C. M. Eigenwillig, G. Palte, D. C. Adler, V. J. Srinivasan, J. G. Fujimoto, and R. Huber, "Real time en face Fourier-domain optical coherence tomography with direct hardware frequency demodulation," *Opt. Lett.* **33**(21), 2556–2558 (2008), <http://www.opticsinfobase.org/ol/abstract.cfm?URI=ol-33-21-2556>.

30. B. R. Biedermann, W. Wieser, C. M. Eigenwillig, T. Klein, and R. Huber, "Dispersion, coherence and noise of Fourier domain mode locked lasers," *Opt. Express* **17**(12), 9947–9961 (2009), <http://www.opticsinfobase.org/oe/abstract.cfm?URI=oe-17-12-9947>.
31. C. M. Eigenwillig, B. R. Biedermann, G. Palte, and R. Huber, "K-space linear Fourier domain mode locked laser and applications for optical coherence tomography," *Opt. Express* **16**(12), 8916–8937 (2008), <http://www.opticsinfobase.org/oe/abstract.cfm?URI=oe-16-12-8916>.
32. C. M. Eigenwillig, W. Wieser, B. R. Biedermann, and R. Huber, "Subharmonic Fourier domain mode locking," *Opt. Lett.* **34**(6), 725–727 (2009), <http://www.opticsinfobase.org/ol/abstract.cfm?URI=ol-34-6-725>.
33. S. W. Huang, A. D. Aguirre, R. A. Huber, D. C. Adler, and J. G. Fujimoto, "Swept source optical coherence microscopy using a Fourier domain mode-locked laser," *Opt. Express* **15**(10), 6210–6217 (2007), <http://www.opticsinfobase.org/oe/abstract.cfm?URI=oe-15-10-6210>.
34. R. Huber, D. C. Adler, V. J. Srinivasan, and J. G. Fujimoto, "Fourier domain mode locking at 1050 nm for ultra-high-speed optical coherence tomography of the human retina at 236,000 axial scans per second," *Opt. Lett.* **32**(14), 2049–2051 (2007), <http://www.opticsinfobase.org/ol/abstract.cfm?URI=ol-32-14-2049>.
35. M. W. Jenkins, D. C. Adler, M. Gargsha, R. Huber, F. Rothenberg, J. Belding, M. Watanabe, D. L. Wilson, J. G. Fujimoto, and A. M. Rollins, "Ultrahigh-speed optical coherence tomography imaging and visualization of the embryonic avian heart using a buffered Fourier Domain Mode Locked laser," *Opt. Express* **15**(10), 6251–6267 (2007), <http://www.opticsinfobase.org/oe/abstract.cfm?URI=oe-15-10-6251>.
36. T. Klein, W. Wieser, B. R. Biedermann, C. M. Eigenwillig, G. Palte, and R. Huber, "Raman-pumped Fourier-domain mode-locked laser: analysis of operation and application for optical coherence tomography," *Opt. Lett.* **33**(23), 2815–2817 (2008), <http://www.opticsinfobase.org/ol/abstract.cfm?URI=ol-33-23-2815>.
37. B. R. Biedermann, W. Wieser, C. M. Eigenwillig, and R. Huber, "Recent developments in Fourier Domain Mode Locked lasers for optical coherence tomography: imaging at 1310 nm vs. 1550 nm wavelength," *J. Biophoton.* **2**(6-7), 357–363 (2009), <http://www3.interscience.wiley.com/journal/122473349/abstract>.
38. V. J. Srinivasan, R. Huber, I. Gorczynska, J. G. Fujimoto, J. Y. Jiang, P. Reisen, and A. E. Cable, "High-speed, high-resolution optical coherence tomography retinal imaging with a frequency-swept laser at 850 nm," *Opt. Lett.* **32**(4), 361–363 (2007), <http://www.opticsinfobase.org/ol/abstract.cfm?URI=ol-32-4-361>.
39. J. A. Filipa, J. W. Walewski, and S. T. Sanders, "Optical beating of polychromatic light and its impact on time-resolved spectroscopy. Part II: Strategies for spectroscopic sensing in the presence of optical beating," *Appl. Spectrosc.* **62**(2), 230–237 (2008), <http://www.opticsinfobase.org/as/abstract.cfm?URI=as-62-2-230>.
40. J. W. Walewski, J. A. Filipa, and S. T. Sanders, "Optical beating of polychromatic light and its impact on time-resolved spectroscopy. Part I: Theory," *Appl. Spectrosc.* **62**(2), 220–229 (2008), <http://www.opticsinfobase.org/as/abstract.cfm?URI=as-62-2-220>.

---

## Introduction

Optical Coherence Tomography (OCT) is a novel biomedical imaging technique for visualizing tissue microstructure *in vivo* [1]. While the first OCT systems used the so called time domain detection (TD-OCT), the demand for higher imaging speeds was one of the main reasons for focusing research on frequency domain OCT (FD-OCT) [2, 3]. At equivalent imaging parameters, FD-OCT provides higher sensitivity [4–6]. As an alternative to spectrometer based FD-OCT systems, FD-OCT systems using rapidly wavelength swept narrow-band light sources (swept source – SS-OCT or optical frequency domain imaging – OFDI [7]) offer several potential advantages: (i) The realization of dual balanced detection is easier, suppressing noise and auto-correlation artifacts; (ii) SS-OCT systems often have a longer ranging depth because of the narrow linewidth and long instantaneous coherence length of the applied laser light sources; (iii) SS-OCT/OFDI systems suffer less from fringe washout caused by sample motion or by rapid scanning of structures with high aspect ratio, and so the performance with respect to signal fading, spatial distortion and blurring can be improved [8].

Since the first demonstration of high speed SS-OCT, huge efforts have been made to push the wavelength sweep repetition rate of the OCT light sources [9–11]. For standard wavelength swept lasers, the length of the resonator limits the maximum wavelength sweep speed (and therefore imaging speed), because the number of possible roundtrips of light in the resonator is reduced and the build-up of saturated lasing from amplified spontaneous emission (ASE) is impeded [12]. Minimizing the laser resonator length enables higher sweep speeds but also enlarges the discrete resonator mode spacing [12, 13]. This can increase intensity noise and ultimately limit the maximum OCT ranging depth, if the laser cavity length is reduced down into the millimeter range.

One solution to this problem is the application of optical circuits without feedback. These resonator-less designs can be broadband light sources with a tunable optical bandpass filter

for post-filtering [12]. Although post-filtering is widely used in all kinds of hyperspectral imaging and microscopy applications, the tight instantaneous bandwidth requirement in OCT of  $\sim 0.1$  nm causes a huge power loss due to the high finesse filtering [14]. Therefore an additional post-amplification can be used to provide sufficient levels of output power. The process of post-amplification of filtered ASE was demonstrated in a very rapidly swept laser source [12], where the tuning rate was above the single roundtrip limit and the laser did not have optical feedback anymore. The problem in this setup was the high ASE background of about 2 mW compared to  $<0.5$  mW of the desired wavelength swept narrow-band signal.

With the demonstration of Fourier Domain Mode Locked Lasers (FDML) [13], the physical limitations of the maximum achievable sweep speed could be overcome and additionally, high output power levels at low ASE background can be achieved. In FDML lasers, an optical delay line in the laser resonator enables to drive the tunable optical bandpass filter synchronously to the round trip time of light in the resonator. The optical bandpass filter can be a rotating polygon mirror in combination with an optical grating [15, 16], a tunable fiber Fabry-Perot filter [17–21] or a tunable active gain element [22]. Record imaging speeds of up to 370,000 lines/s [11], high phase stability [23] and long ranging depths [13] have been demonstrated. FDML lasers have successfully been applied for numerous imaging, sensing and ranging applications [11, 13, 15, 19, 23–37].

The presented wavelength swept ASE source is a new, alternative approach to realize a wavelength swept light source with high power, low ASE and rapid sweeping operation. It should be underlined that it is not a real laser, since no resonator and optical feedback exists. In order to achieve a sufficient output power level and sensitivity for OCT imaging, ASE light alternately passes a linear cascade of *multiple* different gain elements and *multiple* different filter elements. The concept is related to post-filtering and amplification. However, in order to prevent excessive amplification of unfiltered ASE background, the light must be filtered prior to *each* new amplification step, so *several different* filters are required. A crucial factor for optimum performance is to drive the different wavelength filters with an accurate phase delay, to compensate for the light transit time between the filters. Using this technique, no fundamental limit to the sweep speed exists, just like in the case of FDML lasers. However, unlike FDML lasers, the demonstrated setup is fundamentally not limited to discrete drive frequencies. It enables high output power over a continuous range of drive frequencies, limited only by the mechanical response of the filter. Furthermore, the concept is not limited to periodic wavelength sweeps as in FDML. Arbitrary sweep functions can be generated. Additionally, no km long, optical delay fiber is required as in FDML. This reduces cost, especially at wavelengths, where expensive specialty fiber has to be used, e.g. for FDML at 1060 nm. Regarding rapidly swept light sources at 800 nm, the high loss of  $\sim 3$  dB/km and large chromatic dispersion in optical fiber make FDML operation difficult. Therefore the wavelength swept ASE source could be a promising alternative for high speed SS-OCT imaging in particular in the 800 nm or 1060 nm wavelength range.

## 2. Experimental setup and operation

### 2.1 The optical setup

Figure 1(a) shows the fiber-based setup of the demonstrated wavelength swept ASE source at 1300 nm. ASE from the first semiconductor optical amplifier (SOA 1, Covega Corp.) propagates through an optical circulator (CIR, 2 to 3) and is filtered by a piezo actuated, fiber-based tunable Fabry-Perot filter (FFP-TF 1, Lambda Quest, LLC.). The filtered light is directed back to SOA 1 by the circulator (1 to 2). Therefore SOA 1 is used as source for ASE light and simultaneously as a first amplification stage.

The resulting spectrum has to be filtered again with another fiber-based Fabry-Perot filter (FFP-TF 2, Lambda Quest, LLC.) to remove ASE background before the light can be boosted with SOA 2 (Covega Corp.). The polarization state is adjusted with two polarization controllers (PC1 and PC2) because of the polarization dependent gain in the SOAs. The circulator and several isolators (ISO) prevent an amplification of reflected ASE.

## 2.2 The filter control drive waveforms

An arbitrary waveform driver generates two sinusoidal, locked AC voltage signals of same frequency  $f_{\text{drive}}=\omega/(2\pi)$  with a defined, adjustable phase shift with respect to each other. This phase shifted drive signal is very crucial to account for the light transit time  $\tau_{\text{trans}}$  between FFP-TF 1 and FFP-TF 2. Another effect which has to be compensated is the different phase response  $\Delta\phi_R$  of both filters [31] (including contributions of the electronic drivers) at the drive frequency  $f_{\text{drive}}=\omega/(2\pi)$ . Both signals are amplified and superimposed to two independent controllable DC-voltages  $U_{0,1}$  and  $U_{0,2}$  determining the center of the wavelength sweep. The resulting waveforms  $U_1(t)=U_{0,1}+A_1\cdot\sin(\omega t-\phi_1)$  and  $U_2(t)=U_{0,2}+A_2\cdot\sin(\omega t-\phi_2)$  are applied to drive FFP-TF 1 and FFP-TF 2. Because the FFP-TF filters are not identical

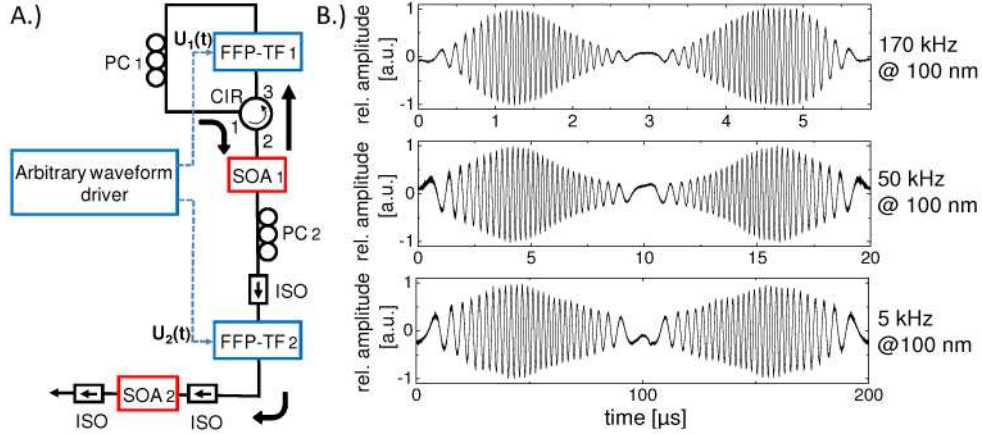


Fig. 1. (a) Setup of the wavelength swept ASE source. The arrows indicate the propagation direction of the light. (b) Interference signal acquired with a Mach-Zehnder interferometer ( $\sim 0.5$  mm delay) for 5 kHz, 50 kHz and 170 kHz filter drive frequency (10 kHz, 100 kHz, 340 kHz effective sweep rate) over a sweep range of 100 nm full width each.

with respect to their free spectral range (FSR) at zero voltage and the voltage response of the piezo actuator, we investigate the optimum drive parameter values in the following. To calculate the required drive waveforms, we consider  $\lambda_k(m_k, t)$  to be the transmission maximum of FFP-TF(k), i.e. the  $k$ th filter in the sequence. The FFP-TF is operated on the  $m_k$ th order. Assuming a linear response  $\alpha_{\omega, k}$  of the piezo actuator in the filter (filter  $k$  at frequency  $\omega/(2\pi)$ ), the refractive index  $n=1$  in the FFP-TFs, and the spacing between the mirror surfaces of filter  $k$  at zero voltage  $d_{0, k}=c/(2\cdot\text{FSR}_k)$ , the following two assumptions can be made: (i) The Fabry-Perot resonator length  $d_k$  is linearly dependent on the applied piezo voltage  $U_k(t)$ , yielding  $d_k(U_k)=d_{0, k}+\alpha_{\omega, k}\cdot U_{0, k}+\alpha_{\omega, k}\cdot A_k\cdot\sin(\omega t-\phi_k)$ . (ii) The Fabry-Perot condition for constructive interference leads to  $\lambda_k(m_k, t)=2d_k/m_k$ . Considering the first two filters,  $k=1$  and  $k=2$ , in order to ensure optimum performance of the wavelength swept ASE source, the condition  $\lambda_1(m_1, t)=\lambda_2(m_2, t-\tau_{\text{trans}}-\Delta\phi_R/\omega)$  must be fulfilled for all times  $t$ . This directly translates to three equations that have to be satisfied simultaneously:

$$\frac{m_2}{m_1} = \frac{d_{0, 2} + \alpha_{\omega, 2} \cdot U_{0, 2}}{d_{0, 1} + \alpha_{\omega, 1} \cdot U_{0, 1}}, \quad (1)$$

$$\frac{m_2}{m_1} = \frac{\alpha_{\omega, 2} \cdot A_2}{\alpha_{\omega, 1} \cdot A_1}, \quad (2)$$

$$\Delta\phi = \phi_1 - \phi_2 = \omega \cdot \tau_{\text{trans}} + \Delta\phi_R. \quad (3)$$

Equation (1) is equivalent to the fact that both center wavelengths  $\lambda_{c,k}(m_k)=(2/m_k)(d_{0,k}+\alpha_{0,k}\cdot U_{0,k})$  must be matched, Eq. (2) implies equal full sweep ranges  $\Delta\lambda_k(m_k)=4\alpha_{0,k}A_k/m_k$  and Eq. (3) describes the condition for the phase delay. Considering only these three equations, for every combination of FFP orders  $m_1$  and  $m_2$ , there is a solution yielding a desired  $\lambda_c$  and  $\Delta\lambda$ . Nevertheless, since the piezo of the FFP-TF becomes nonlinear for too high input voltages, more conditions emerge that can make the problem unsolvable. Therefore, in order to avoid high  $U_{0,k}$  or  $A_k$ , it can make sense to choose different orders  $m_k$  if the FSRs of both filters at zero voltage are differing considerably. A rough estimation of the required accuracy for the filter parameter adjustment ensuring optimal operation is  $\sim 0.2^\circ$  for  $\Delta\phi$  and  $\sim 0.2\%$  of  $U_{0k}$  and  $A_k$ .

In our setup, the FSR (zero voltage) of FFP-TF 1 was measured to be 22.2 THz, the FSR (zero voltage) of FFP-TF 2 was 27.2 THz. This difference is mainly compensated by matching the order  $m_1=11$  (FFP-TF 1) with the order  $m_2=9$  (FFP-TF 2). At a filter drive frequency  $f_{\text{drive}}=50$  kHz, the DC voltages are  $U_{0,1}=11.6$  V and  $U_{0,2}=10.5$  V, yielding  $\lambda_c\sim 1302$  nm, the AC voltages  $A_1=1.4$  V and  $A_2=0.9$  V result in  $\Delta\lambda=100$  nm.

Due to thermal drift, non-linearity of the PZT and other parasitic effects, it is difficult to exactly predetermine all parameters to operate the source. Therefore, as startup procedure in our experiment, all parameters were optimized by slowly increasing the sweeping bandwidth while monitoring the power output of the source and the symmetry of both sweep directions.

### 3. Performance of the wavelength swept ASE source

#### 3.1 Spectrum and output power

To demonstrate the good performance of the wavelength swept ASE source over a wide range of filter drive frequencies, we measured the interference signal (Fig. 1(b)) from a Mach-Zehnder interferometer with 0.5 mm arm length mismatch. The signals are plotted over one filter drive cycle (both sweep directions) for 5 kHz, 50 kHz and 170 kHz filter drive frequency at a full sweep range of 100 nm each. This corresponds to sweep rates of  $2\times 5$  kHz=10 kHz,  $2\times 50$  kHz=100 kHz and  $2\times 170$  kHz=340 kHz. The frequencies were chosen close to mechanical resonances of the filter to prevent heating and drift. In all cases, a average output powers of  $\sim 1.2$  mW after FFP-TF 2 and 50 mW after the last isolator have been achieved. In spite of the fact that the wavelength swept ASE source is critically sensitive to the setting of all filter drive parameters (see section 2), a stable operation could be observed for up to half an hour at  $2\times 170$  kHz and up to many hours at  $2\times 5$  kHz and  $2\times 50$  kHz. During this time, the ASE source could be used for imaging until filter drift effects led to a reduction of the output power and the sweeping bandwidth. Then a readjustment, mainly of the DC-voltage, was required. A closed feed-back loop to control the DC-voltage may enable stable, adjustment free operation at any frequency.

Figure 2(a) shows the spectrum of the wavelength swept ASE source at a filter drive frequency of 50 kHz and 100 nm full sweep width (50 mW average output power) measured with an optical spectrum analyzer (OSA). The broad background results from ASE, emitted by SOA 2. The sharp peak features at the edges of the spectrum are due to the non-linear, sinusoidal drive, they do not occur in the time traces (see Fig. 1(b)).

#### 3.2 Required accuracy of the phase delay setting

In order to investigate the required accuracy of the phase delay between the filter drive waveforms, Fig. 2(b) shows the measured relative output power after FFP-TF 2 for different filter phase delay values  $\Delta\phi_F=\Delta\phi+\Delta\phi_R$  (red dots), being calculated from the difference in phase of the applied voltage  $\Delta\phi$  and the difference in filter phase response  $\Delta\phi_R$ . The power was averaged over one entire intensity trace, including forward (short to long wavelengths) and backward sweep. The full sweep range was 100 nm, the filter drive frequency 50 kHz. The mechanical phase response of both filters was measured at a drive frequency of 50 kHz with the method described in [31]. We observed a difference in the phase response of  $\Delta\phi_R=-1.9^\circ\pm 0.4^\circ$ . Figure 2(b) is corrected for the different mechanical response. Thus, the

resulting curve has its maximum at  $\Delta\phi_F=1.6^\circ\pm 0.4^\circ$  ( $\Delta\phi=3.5^\circ$  phase delay in applied voltage) which is in good agreement with Eq. (3). The transit time  $\tau_{\text{trans}}$  of light between the two filters is 102 ns in the setup, equivalent to 20.8 m of optical fiber or  $1.8^\circ$  phase shift at 50 kHz. This indicates that the phase shifted control of the two filters leads to an efficient operation by compensating light propagation effects. The full width at half maximum (FWHM) of the measured curve in Fig. 2 is  $0.95^\circ$  which implies a temporal width of 52.8 ns at 50 kHz. For a filter drive frequency of 5 kHz, this result translates to a temporal width of 528 ns, at 170 kHz of only 15.5 ns. The axis at the top of the graph shows the corresponding filter wavelength shift for a full sweep width of 100 nm assuming a mean filter sweep speed of 100 nm/10  $\mu$ s (triangular, linear sweep). In order to obtain the theoretically expected drop of the average power (Fig. 2(b), black line), the instantaneous transmission spectra of both filters have to be convoluted with each other. For simplification, both spectra were measured only for those

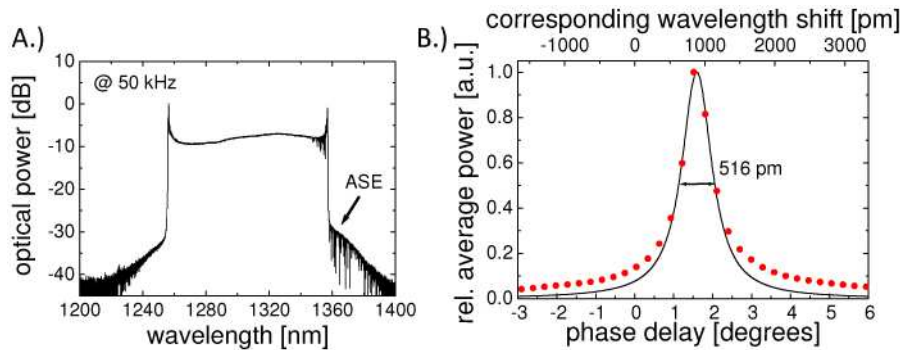


Fig. 2. (a) Output spectrum of the wavelength swept ASE source measured with an OSA at 50 kHz filter drive frequency (100 nm full sweep width) at an output power of ~50 mW. (b) Measured relative average power after FFP-TF 2 over the applied filter phase delay at a filter drive frequency of 50 kHz (red dots). The black line represents the relative power drop expected from theory. Additionally, the corresponding wavelength shift (100 nm full sweep range, assuming linear drive) is displayed as second x-axis.

wavelengths providing the smallest instantaneous linewidths in the center of the sweep. The FWHM is 255 pm for FFP-TF 1 at 1330 nm and 284 pm for FFP-TF 2 at 1310 nm, yielding a FWHM of 516 pm ( $0.93^\circ$ ) after convolution. Good agreement with the measured data is observed. It should be noted that *this is not the* instantaneous linewidth (see chapter 4.3), but the sensitivity with respect to timing. The deviation between measurement and theory in Fig. 2(b), mainly in the wings of the curve, is probably due to an increase of the instantaneous linewidth and a decrease of the filter sweep speed towards the turning points of the filter, making the phase delay adjustment less critical. Thus, the edges of the spectrum make a dominant contribution to the average power in case of large phase detuning.

In summary, directly after FFP-TF 2, the acquired accuracy to set the delay time of the two filter drive signals is only determined by the properties of both filters (instantaneous linewidths) and the filter drive speed. After SOA 2, saturation effects also play a role, making the relative average power less critical to phase delay ( $\sim 3^\circ$  FWHM, 50 kHz). Nevertheless, for an optimum performance of the wavelength swept laser source, it is practical to optimize the drive parameters under consideration of the power after FFP-TF 2.

### 3.3 Instabilities and partial parasitic lasing at low frequencies

One feature of the demonstrated setup is the dual use of SOA 1, on the one hand as ASE source and on the other hand as a first amplification stage. This concept reduces the number of gain elements, no super luminescent diode (SLD) or additional SOA is required as primary broadband light source for seeding the amplification chain. Because of the dual use of SOA 1, saturation must be avoided to prevent a suppression of ASE light. Since in our case the typical average input power  $P_{\text{in}}$  to SOA 1 is about 10  $\mu$ W, the small signal gain  $G$  is  $\sim 30$  dB and the

saturation power of the SOA is specified as 68 mW, saturation should be no problem for typical operation. The condition  $P_{in} \cdot G \ll P_{sat}$  is fulfilled.

However, at low drive frequencies, we observed a characteristic feature that results from the double pass through SOA 1. The four traces in Fig. 3 show the transient optical power at different sweep frequencies over one filter drive cycle each (after the last isolator, acquired with a 150 MHz photo detector). Each trace corresponds to 100 nm full sweep width and an average output power of  $\sim 40$  mW. In contrast to the filter drive at 50 kHz (Fig. 3(a)), the curve at 5 kHz (Fig. 3(b)) exhibits strong, parasitic modulations and high noise. At 1 kHz filter drive (Fig. 3(d)) the intensity modulation are even worse. In all three cases (A, B, D) the average input power  $P_{in}$  to SOA 1 is  $\sim 8 \mu\text{W}$ . The measurements show that the amplitude of

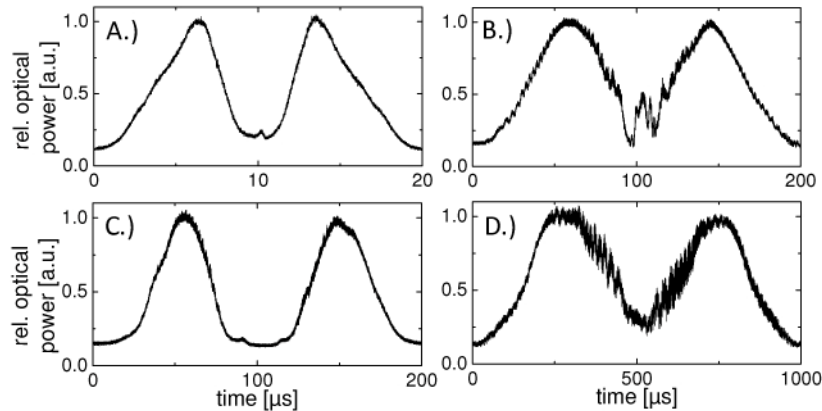


Fig. 3. Relative optical power for forward and backward sweep measured at 100 nm full sweep width and  $\sim 40$  mW output power. The filter drive frequency is 50 kHz (a), 5 kHz (b and c) and 1 kHz (d); the average input power to SOA 1 is  $\sim 8 \mu\text{W}$  (a, b and d) and  $\sim 4 \mu\text{W}$  (c).

the power modulations is increasing with smaller wavelength sweep speed, slow sweeping causes higher noise. Besides the noise dependence on the filter drive speed, the observed noise also depends on the average input power  $P_{in}$  to SOA 1. A considerable reduction of the intensity modulations at 5 kHz drive can be achieved by reducing  $P_{in}$  to  $\sim 4 \mu\text{W}$  and increasing the amplification of SOA 2, in order to achieve the same output power (compare Fig. 3(c) and Fig. 3(b)). To analyze the origin of the observed instabilities, we calculated the Fourier spectrum of the noise. We observe broad maxima at  $\sim 10.3$  MHz and  $\sim 11.1$  MHz, for sweep rates of  $2 \times 1$  kHz and  $2 \times 5$  kHz, respectively. These values correspond very well with the optical path length of 18.4 m, which is the length from SOA 1 to the circulator (port 2), to the FFP-TF 1, to the polarization controller, to the circulator (port 3) and finally back to SOA 1. This observation implies that residual optical feedback from the back facet of SOA 1 causes a resonance. Since in the described circuit light experiences two amplifications by the SOA, the resulting total gain of up to 60 dB is high enough for partial parasitic lasing, considering typical SOA facet reflectivities of  $10^{-5}$ . Since the light passes through the filter, this partial parasitic lasing can only build up for very slow sweep rates of the filter, providing enough round trips. The effect is equivalent to the sweep rate limitation in standard swept laser sources [12]. So, by reducing the gain in SOA 1, this partial parasitic lasing can be avoided. Also, for high sweep rates, the problem does not occur. Increasing the length of the described circuit will also reduce this effect by increasing the transit time. Then, the effect of parasitic lasing will occur at even lower frequencies.

#### 4. Sensitivity and roll-off characteristics

##### 4.1 Coherence and sensitivity

In order to investigate the coherence properties of the wavelength swept ASE source, the roll-off characteristics have been analyzed. We acquired interference signals with a dual balanced

Mach-Zehnder interferometer for different delays at a filter drive frequency of 50 kHz and a full sweep range of 100 nm. The recorded fringe signals were Fourier transformed over forward sweeps (10  $\mu$ s) after numerical resampling but without apodization and the resulting point spread functions (PSF) are plotted in Fig. 4(a) (lines) against OCT ranging depth, i.e. 0.5x the arm length mismatch of the Mach Zehnder interferometer. The logarithmic scale was adjusted such that the peak values correspond to the maximum achievable sensitivity in OCT application, assuming a lossless imaging setup and no power attenuation. The maximum sensitivity was determined to be 120.6 dB at a ranging depth of 0.25 mm for an average output power of 48 mW.

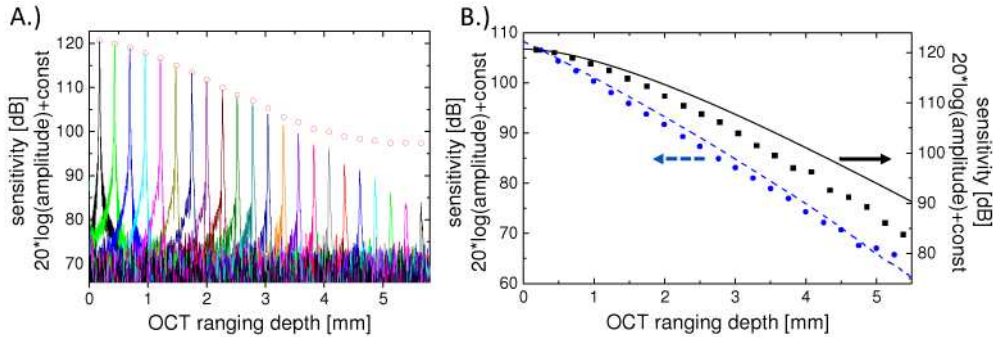


Fig. 4. (a) Logarithmic plot of the measured PSFs (lines) of the wavelength swept ASE source at 50 kHz (100 nm full sweep width), representing the measured sensitivity against different OCT ranging depths. The red circles indicate the drop of fringe contrast. (b) Logarithmic plot of the maxima of the measured PSFs over OCT ranging depth after the second pass through SOA 1 (blue circles, sensitivity left) and at the output of the wavelength swept ASE source after SOA 2 (black squares, sensitivity right). The blue, dashed line and the black, solid line indicate the corresponding drop of sensitivity, expected from theory.

The red circles represent the drop of the interference contrast extracted from the interference signal envelope. No significant difference between forward and backward sweep could be observed. The maximum resolution (3 dB Gaussian fit) was measured to be  $\sim 12 \mu$ m in air, the dynamic range was  $\sim 50$  dB.

#### 4.2 Fringe visibility, optical phase noise and incoherent background

There are two remarkable features in Fig. 4(a). First, we can observe that neither the width of the PSFs nor the amount of side lobes change significantly over depth, even though the measurement range covers a total roll-off of  $\sim 40$  dB. All PSFs appear sharp with negligible pedestal, only the amplitude decreases. It should be noted that the calibration signal for time to optical frequency resampling was only recorded once, before all the measurements. The fact that all PSFs are sharp even for long delays indicates that there is no drift, deviation, or low frequency oscillation on the evolution of the instantaneous center wavelength. Each sweep is very repeatable, the instantaneous wavelength does not jitter around the mean time dependent wavelength evolution, which can be the case in standard swept laser sources (random stepwise tuning). This fact may make the source highly suitable for any measurement, where an accurate knowledge of the center wavelength is required, like for fiber Bragg grating (FBG) sensing [20, 21].

The second observation in Fig. 4(a) is that at depths larger than  $\sim 3$  mm, the red dots for the fringe visibility do not lie on the peaks of the PSFs. The roll-off over depth of the fringe visibility is significantly slower than for the PSFs. This is different from the situation found in standard wavelength swept lasers [38] or FDML lasers [31, 32], where over most of the measurement range the roll-off of the fringe visibility and the peaks of the PSFs is similar.

For the situation in the wavelength swept ASE source, we propose the following model. The considerations are similar to the more detailed analysis of *intensity noise* in [39,40], however, here we discuss the influence of *phase noise*. In our case, relative intensity noise is

cancelled out by the dual balanced differential detection. The FWHM of the combined filters is  $\sim 0.18$  nm, i.e.  $\sim 31$  GHz optical linewidth at 1310 nm. This means, over a time of  $\sim 1/31$  GHz = 32 ps, phase and amplitude of the optical field are stable and can interfere. The optical field can be split and one part can be delayed by  $\pm 16$  ps with respect to the other field. If we consider the situation at a measurement depth of 5 mm (10 mm optical delay), the two optical fields are shifted by 33 ps with respect to each other and interfere. Due to the large temporal shift, there is no well defined phase relation between the two fields, however, the resulting, arbitrary phase difference stays constant for up to about 32 ps. If the dual balanced differential detector would be fast enough, a noise like signal with contributions up to 31 GHz would be observed. We can assume a flat noise spectrum from the SOA, so the measured noise power at the output of our 350 MHz detector will be approximately  $31 \text{ GHz}/350 \text{ MHz} = 89$  times smaller, i.e.  $\sim 19$  dB.

In a time domain picture, a signal is generated on the dual balanced differential detector by coherent contributions of the light field, incoherent background is cancelled. The coherence time is  $\sim 32$  ps, i.e. the time over which a stable signal at the photodiode can be generated. After an average time of 32 ps, the phase relation is lost, that means every 32 ps another output value is measured at the photo-receiver. However, since the photodiodes and the detection system have an analog bandwidth of only 350 MHz,  $\sim 89$  of these 32 ps intervals will be averaged incoherently. Because the signals of each of the 32 ps intervals have no phase relation, they add up incoherently and the voltage amplitude will be  $\sim \sqrt{89} = 9.4$ , i.e. 19 dB lower than a coherent sum, like at short delays. This means a random signal amplitude with  $-19$  dB will always remain at ranging depth longer than the instantaneous coherence length.

If we now compare the roll-off in fringe visibility for 0.25 mm ranging depth and 5.6 mm ranging depth, we observe 120.6 dB and 97.4 dB, respectively. The difference of 23.2 dB has the same order of magnitude than the calculated value above of  $\sim 19$  dB, underlining the link between optical filter bandwidth, analog detection bandwidth and incoherent noise background. This means, applying a more narrowband filter will increase the instantaneous coherence length, but it will also increase the incoherent noise floor. This fact is important for the design of OCT and other coherent ranging systems, operated at the edge of the coherence performance of the applied light source.

The described link between instantaneous optical bandwidth and minimum noise floor should be universal and also applies to FDML lasers and conventional swept laser sources. However, in the case of lasers, the assumption of a white and flat noise background cannot always be made. Typically, in lasers higher noise at the cavity roundtrip frequency and the harmonics is observed. Even though the observed noise is usually relative intensity noise (RIN), phase noise and coherence properties might also be affected.

#### *4.3 Improved performance by double filtering: reaching the shot noise limit*

Another important feature of the wavelength swept ASE source is the advantage of an additional last filtering and amplification step, even though without it, setup and operation of the source would be even less complex. Therefore, in Fig. 4(b) the roll-off performance directly after the second pass through SOA 1 (maxima of PSFs, blue circles) is compared to the one of the wavelength swept ASE-source after FFP-TF 2 and SOA 2 (maxima of PSFs, black squares). The maxima of the PSFs represent the measured sensitivity. The maximum measured sensitivity of the wavelength swept ASE source after FFP-TF 2 and SOA 2 is 120.6 dB (48 mW). It exceeds the value obtained after SOA 1, which is measured to be 106.5 dB (0.25 mm OCT ranging depth) at 12 mW average output power. The shot noise limited sensitivity [6] for the wavelength swept ASE source after FFP-TF 2 and SOA 2 is 121.3 dB which is only 0.7 dB higher than the measured value. The theoretical value after SOA 1 is 115.4 dB which is 8.9 dB larger than the measured value. The observed difference is mainly due to the large ASE background directly after SOA 1, which contributes 80% of the total power, only 20% is coherent signal contribution. This discrepancy is due to the fact that with an input power of  $\sim 1$  mW, SOA 2 is highly saturated, whereas the input power to SOA 1

(typically  $\sim 10 \mu\text{W}$  in our setup) is limited by the available power in the ASE spectrum and the narrow FWHM of the FFP-TF 1 transmission, preventing saturation. This means that the shot noise limit can only be reached with 2 SOAs and 2 filters, reducing ASE background.

In addition to higher power and reduced ASE background (yielding higher sensitivity), another advantage of using 2 filters is the improved coherence. At an imaging depth of 4 mm, a 7.5 dB difference in sensitivity is observed (Fig. 4(b)) due to the second filtering event. The blue dashed line (after SOA 1) and black solid line (after FFP-TF 2 and SOA 2) represent the roll-off expected from theory. They are calculated by a fast Fourier transform (FFT) of either the transmission spectrum of FFP-TF 1 (255 pm instantaneous linewidth (FWHM) at 1330 nm) or FFT of the product of both transmission spectra (FFP-TF 1 at 1330 nm and FFP-TF 2 at 1310 nm with an instantaneous linewidth (FWHM) of 180 pm). Good agreement with the measured data is observed, in particular for the operation after SOA 1. The deviation from the solid curve can be caused by a non-perfect drive parameter adjustment. Another possible explanation for the slight deviation of both curves is the increasing transmission bandwidth of the FFP-TFs towards the edges of the spectrum (e.g. 388 pm FWHM at 1250 nm vs. 255 pm FWHM at 1330 pm for FFP-TF 1), degrading the coherence properties. Due to the saturation of SOA 2, the relative power in the edges of the spectrum is increased compared to the spectrum after SOA 1. Thus, a larger instantaneous linewidth at the edges of the spectrum might have a larger influence on the coherence after SOA 2 than after SOA 1, explaining the higher deviation from the expected curve.

In summary, the measurements are indicating that the roll-off characteristics are only determined by the transmission spectra of the filters, if an optimum drive parameter setting is assumed. The roll-off of the demonstrated wavelength swept ASE source cannot match that of FDML operation, where multiple filtering events occur. The R-number (compare [30]) of the wavelength swept ASE source is determined to be 0.13 mm/dB (linear fit from 0.75 mm to 5.5 mm). For FDML lasers with comparable filter specifications and SOA gain media we reported  $R \sim 0.3$  mm/dB [31],  $R = 1.4$  mm/dB [30] and  $R \sim 0.4$  mm/dB [32]. Nevertheless, the coherence properties are comparable to standard wavelength swept laser sources driven at high wavelength tuning speeds, where only the filter bandwidth determines the instantaneous coherence length [12]. It may be sufficient for many applications, like OCT of the human retina, where a ranging depth of  $\sim 2$  mm is sufficient. Furthermore, in order to push the roll-off performance, one or even two filters with a considerably narrower instantaneous transmission spectrum could be used instead, tolerating the resulting drawback of reduced output power. The requirement for the finesse of the filters would be relaxed, if two filters with narrow but slightly different FSR were used in order to achieve very narrow transmission bandwidth (Vernier tuning). Furthermore, the bandwidth of the first or alternatively the second filter may be increased, to make the phase adjustment less critical while still maintaining a narrow linewidth.

## 5. Relative Intensity Noise (RIN)

The RIN is a very important parameter to characterize light sources. The RIN properties are affecting the dynamic range in OCT application and may influence the image quality. RIN is the ratio of the standard deviation of the optical power  $\delta P$  over the mean optical power  $P$ . As described in [30], for periodically swept light sources, it is a reasonable and the most conservative way to analyze the power fluctuations between different sweeps at defined points in time (inter-sweep noise), rather than power fluctuations within one sweep over a sliding time window (intra-sweep noise). For the following measurements the optical power was measured with a photo detector (150 MHz analog bandwidth, Thorlabs), the resulting signal was lowpass filtered at 100 MHz and sampled with a 200 MSamples/s, 12 bit analog to digital converter card (ADC). 100 records, each consisting of 2000 samples, were acquired, each record covers one backward sweep. Thus, RIN (inter sweep noise) can be calculated for every sample in the record and hence assigned to individual wavelengths. The measured inter-sweep noise covers a bandwidth up to the system's 100 MHz analog bandwidth [30].

For a better understanding of the differences, the RIN performance of the presented wavelength swept ASE source is directly compared to the RIN of an FDML laser. Up to now, a quantitative determination of RIN for FDML lasers has only been reported at 1550 nm [30]. The FDML laser used for this comparison (1310 nm) was built in a sigma ring configuration. The complete laser, except for the delay line, consists of polarization maintaining (PM) fiber.

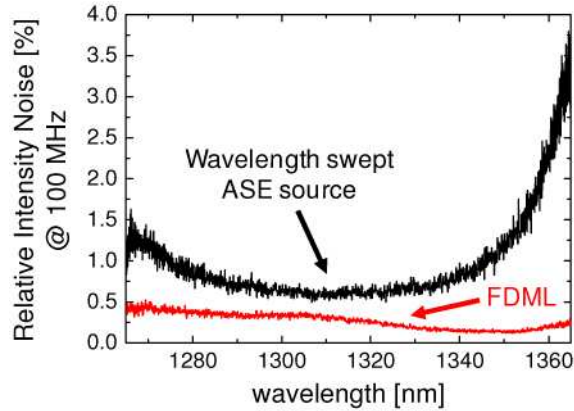


Fig. 5. RIN value versus wavelength at a filter drive frequency of 54.6 kHz and a full sweep range of 100 nm at an analog bandwidth of 100 MHz. The black line represents the RIN of the wavelength swept ASE source, the red line represents the RIN of the FDML laser.

A PM version of the FFP-TF is used (LambdaQuest, LLC.). 30% of the power was coupled out between the SOA (Covega Corp.) and the delay line, 30% after the FFP-TF and the delay line. For the RIN analysis, the output after the SOA was analyzed. In order to match the operation parameters as well as possible, both, the FDML laser and the wavelength swept ASE source were driven at the fundamental FDML frequency of 54.6 kHz (2x bidirectional sweep duration of 9.2  $\mu$ s) over a full sweep width of 100 nm and at a center wavelength of 1315 nm. The average output power of  $\sim$ 32 mW was attenuated to  $\sim$ 1.3 mW on the detector in both cases. For FDML operation, the choice of the accurate drive frequency is important for an optimum RIN performance. Thus, the RIN was measured over a frequency range of 600 Hz with a step size of 1 Hz. The frequency yielding the best RIN performance was chosen. When detuning the wavelength swept ASE source by several 10 Hz, the RIN is almost independent of the drive frequency; small differences are due to frequency dependent differences of the filter phase response (different filter phase delays). Here, the frequency with the highest average output power was chosen.

In Fig. 5, the measured RIN value is plotted versus wavelength. The black line shows the RIN of the wavelength swept ASE source for a frequency of 54.680 kHz, the red line shows the RIN of the FDML laser at 54.574 kHz. The RIN value averaged over all wavelengths is 0.28% for the FDML laser and 1.33% for the wavelength swept ASE source. Obviously, the RIN performance of the FDML laser is exceeding that of the ASE source over the whole sweep spectrum, which is not surprising due to quasi-stationary operation in FDML [13]. The average relative ratio of both RIN values is  $\sim$ 4.8, the smallest is found at 1310 nm with 1.7 and the largest value of  $\sim$ 14.3 is identified at the long wavelength side of the spectrum at 1365 nm. The reason for the strong increase in RIN of the wavelength swept ASE source at long wavelengths is unclear. It can be assumed that the last saturated amplification step in SOA 2 is considerably improving the RIN performance for the ASE source.

In standard wavelength swept lasers, RIN is considerably increasing with filter sweep speed [12, 30]. The RIN performance of the wavelength swept ASE source is comparable and may be even superior to standard wavelength swept lasers at high imaging speeds, because the lack of optical feedback prevents the appearance of a dominant noise at the laser cavity roundtrip frequency.

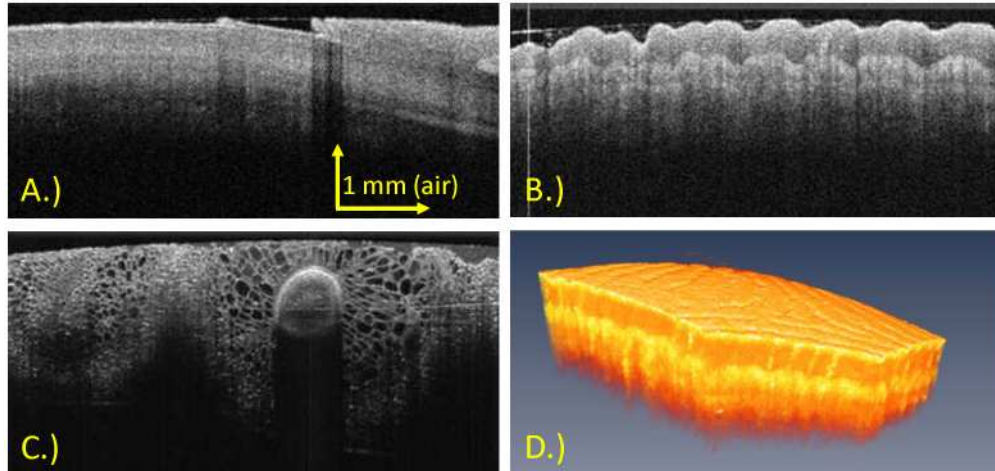


Fig. 6. OCT images acquired with the wavelength swept ASE source at 50 kHz A-line rate and 100 nm full sweep range. (a) human finger (nail fold); (b) human finger; (c) 2D OCT image of a cucumber (10x averaged); (d) Rendered 3D representation of a human finger.

## 6. OCT imaging

To demonstrate the OCT imaging performance of the wavelength swept ASE source, Fig. 6 shows OCT images at a filter drive frequency of 50 kHz and a full sweep range of 100 nm. The input power into the OCT setup was  $\sim 30$  mW resulting in an average power of 10 mW on the sample. The transversal resolution was  $\sim 17$   $\mu\text{m}$ , the measured sensitivity in the setup was  $\sim 110$  dB. Signals from the detector were sampled at 400 MSamples/s with a 12 bit ADC. The data is numerically resampled for equidistant frequency spacing before the Fourier transform. Figure 6 shows 2D OCT-images (1024 lines, 5.4 mm) of the nail fold of a human finger in vivo (no averaging, Hanning apodized) (A), skin of a human finger (no averaging, Hanning apodized) (B) and a cucumber (10x averaged, Hanning apodized) (C). Figure 6(d) is a 3D reconstruction of an OCT data set of human skin (finger) consisting of 500 frames, 512 lines and 2000 axial pixels. The image quality is comparable to other high speed swept source OCT images. The images exhibit good contrast and penetration.

## 7. Conclusion and outlook

In conclusion, we presented an alternative approach to realize a rapidly wavelength swept light source for high-speed OCT imaging and sensing. A sequence of optical gain elements and tunable bandpass filters, which are driven with a defined phase delay, represent an optical circuit without feedback, overcoming physical limitations in sweep repetition rate. In analogy to FDML lasers, no fundamental limit to sweep speed exists, but in contrary, an operation over a continuous range of drive frequencies is possible. We demonstrated a wavelength swept ASE source at 1300 nm consisting of two SOA gain elements and two FFP-TF filter elements. We obtained an average output power of 50 mW. A full sweep range of 100 nm at 10 kHz, 100 kHz and 340 kHz sweep rate was achieved.

We showed that two filtering and amplification steps are necessary to achieve shot noise limited detection in OCT, to suppress ASE and to improve the coherence properties of the light source. We present a physical model for the connection between the optical filter bandwidth, the analog detection bandwidth and the observed incoherent background noise in OCT application. OCT imaging was demonstrated at 50 kHz line rate with good image quality, contrast and penetration.

In the future, the demonstrated technique may be attractive for swept light sources at 800 nm and 1060 nm, where high fiber loss and dispersion impede the realization of FDML lasers. Since no km long delay fiber is required, the wavelength swept ASE source might be very promising for ophthalmic high-speed SS-OCT. By optimizing the bandwidth of the

different optical bandpass filters, the performance of the source may be further optimized. Non-equal values may be chosen to achieve good coherence properties and robust operation. Since the source appears to have extremely repeatable temporal tuning characteristics, it may be very suitable for sensing applications where a highly accurate measurement of spectral features is required, e.g. for fiber bragg grating sensors.

### **Acknowledgments**

We would like to acknowledge support from Prof. W. Zinth at the Ludwig-Maximilians-University Munich. This research was sponsored by the Emmy Noether program of the German Research Foundation (DFG - HU 1006/2-1) and the European Union project FUN-OCT (FP7 HEALTH, contract no. 201880).